15th AIAA/CEAS Aeroacoustics Conference (30th AIAA Aeroacoustics Conference)
11 - 13 May 2009, Miami, Florida

AIAA 2009-3165

Energy-Based Acoustical Measurements of Rocket Noise

Kent L. Gee[1], Jarom H. Giraud[2], Jonathan D. Blotter[3], Scott D. Sommerfeldt[4]
Brigham Young University, Provo, UT, 84602

Energy-based acoustical measurements are investigated in the context of more fully characterizing rocket noise source regions. Near-field measurements made on statically fired GEM-60 motors are described and the performance of two types of four-microphone tetrahedral probes is discussed. Vector intensity plots reveal the magnitude and directionality of the near-field sound radiation as a function of frequency, position, and time in the plume.

I. Introduction

THE development of the next-generation space flight vehicles has prompted renewed interest regarding source characterization and near-field propagation models of rocket noise. This source characterization is required to determine the vibroacoustic impact on flight hardware and structures in the vicinity of the launch pad. Brigham Young University has been involved in an effort to develop and validate an energy-based acoustic probe suitable for use in rocket fields, in particular the RS-68B engine to be used on the Ares V vehicle.

Energy-based acoustical measurements require estimation of both the collocated acoustic pressure and the three-dimensional particle velocity. From the pressure, a scalar, and the particle velocity vector, a number of energy-based quantities can be calculated, including vector acoustic intensity, specific acoustic impedance, potential, kinetic, and total energy densities, and the Lagrangian density. Knowledge of one or more of these quantities may provide important information about the source characteristics that acoustic pressure alone cannot.

The relative importance of these different quantities depends on the location of the measurement relative to the source. In the acoustic near field, there is a nonzero phase difference between the pressure and particle velocity. The specific acoustic impedance, energy densities, Lagrangian density, and reactive intensity have important meanings close to the acoustic source. However, as the acoustic far-field is approached and the propagating wavefront becomes locally planar, the specific acoustic impedance approaches the characteristic impedance of the medium, the kinetic, potential, and total energy densities can be calculated from the pressure alone, and the Lagrangian density and reactive intensity approach zero.

If acoustic near-field measurements are not feasible, one energy-based quantity still yields significantly more information regarding the source than a pressure microphone measurement. This is the active, or propagating, *vector* intensity. The word vector is emphasized because the term “intensity” has traditionally held a far-field, magnitude-only meaning (i.e. proportional to squared pressure) within the jet aeroacoustics community. In the acoustic near-field of the source, the total complex intensity is comprised of active and reactive portions, where the active part is the time-averaged product of the pressure and the in-phase component of the particle velocity. The reactive component of the intensity represents the near-field transfer of energy from the source to the fluid and from the fluid back to the source.

Although acoustic intensity has been used in a wide variety of applications for determining source characteristics, and a book has been written solely on the topic,[1] it is rarely employed in aeroacoustics settings. Jaeger[2] used two-dimensional intensity vectors in a ray-based method to localize sources in a subsonic jet. Beyond that, the vector intensity work in the aeroacoustics regime has been in one dimension. Ventakesh *et al.*[3] utilized a one-dimensional intensity probe to validate a new type of beamforming algorithm for distributed sources, but few details are provided on how it was used to determine source locations. Finally, Yu *et al.*[4,5] have proposed a method

---

[1] Assistant Professor, Dept. of Physics and Astronomy, N-243 Eyring Science Center, kentgee@byu.edu, AIAA Member.

[2] Undergraduate Research Assistant, Dept. of Physics and Astronomy, N-283 Eyring Science Center.

[3] Professor, Dept. of Mechanical Engineering, 435 Crabtree Technology Bldg.

[4] Professor, Dept. of Physics and Astronomy, N-181, Eyring Science Center.

for reconstructing sources that relies on a measurement of acoustic intensity in the direction normal to the measurement surface.

Determination of acoustic intensity and other energy-based quantities requires estimates of both the pressure and the particle velocity at a point in space. Although a commercial particle velocity sensor exists (the so-called "microflown"), the more common method for estimating particle velocity is to use two closely spaced, well-matched microphones. Assuming time harmonic behavior, the gradient between the two microphones can be related to the particle velocity for each frequency by using a linearized Euler's equation. Therefore, the vector intensity along a given direction can be obtained by perfoming a centered finite difference between the two microphones and an average of the pressures at the microphones to obtain both the particle velocity and pressure at the center of the probe. By using orthogonally oriented pairs of microphones, particle velocity estimates can be obtained in two or three dimensions. In practice, the number of microphones for three-dimensional velocity estimates can be reduced from six to four non-coplanar microphones by additional signal processing as described by a number of authors[6-8].

In the special case where propagating wavefronts may be considered locally planar across the probe, there is an alternative to the finite-difference technique of estimating particle velocity using two or more microphones. This method[9] utilizes transfer functions between microphones to estimate a time-of-flight (manifest by a phase difference) and determine the wavevector magnitude and direction as a function of frequency. By assuming locally planar propagation at the center of the probe, the wavevector and the pressure magnitude may be used to calculate acoustic intensity. Although limited to locally planar propagation, it is not as sensitive to phase and amplitude mismatch errors as the finite-difference method at low frequencies and is not subject to pressure averaging bias errors as the sensor separation distance relative to a wavelength increases. The "wavevector" method[9] is employed in this paper to calculate vector intensity results from four-microphone probes in propagating rocket noise fields.

II. Probe Prototype Descriptions

Two different types of probes were tested in the rocket noise field, the GRAS-built NASA probe prototype that was the primary motivation for these tests, and an in-house "external frame" tetrahedral probe that used four condenser microphones. The probe prototypes are displayed in Fig. 1. The NASA-probe prototype consists of four matched GRAS 6.35-mm 40BH pressure microphones in a 2.54-cm diameter machined aluminum sphere. The four preamplifiers for the microphones are located inside the sphere. The GRAS 40BH microphones were used because of their low sensitivities (~0.5 mV/Pa) and large maximum sound pressure level (194 dB re 20 μPa). A standard 7-pin LEMO cable was used to provide power to the microphones and carry the four signals to a custom breakout cable that fed into two dual-channel GRAS 12AA power supplies. These supplies provide the 200V polarization voltage for the microphones and the 120V preamplifier supply. This supply voltage (rather than 15 or 28 V) was required because the large pressures incident on the microphone faces could otherwise saturate the preamplifiers.

The external frame probes were constructed to hold the microphones in a regular tetrahedron and at the same time, accommodate multiple intermicrophone spacings. Two types of microphones were used in these probes. One probe used GRAS 40BH microphones, 26AC preamplifiers, and 12AA power supplies. In effect, this probe utilized the same hardware as the NASA probe prototypes. The second type of probe used constant-current-powered prepolarized GRAS 6.35-mm 40BD pressure microphones with specially reduced sensitivities that allows peak pressures slightly greater than 20 kPa (180 dB re 20 μPa) to be recorded before the 10 V 26CB preamplifier limit is reached.

Displayed in Fig. 2 is a regular tetrahedron aligned such that microphones 2 and 4 are parallel to the y axis. The positive x axis points from microphone 3 to the midpoint between microphones 2 and 4 and the positive z axis points from the plane containing microphones 2, 3, and 4 upward towards microphone 1. This is the geometry for the NASA spherical probe prototype. The only difference for the external frame tetrahedral probe is that because microphone 1 is below rather than above the horizontal plane containing the other microphones, the direction of the z-axis vector (when dealing with vector quantities) must be switched. Other than that, the data from the two probes can be processed the same. However, because the vertical intensity component is not considered in this paper, this is not a critical issue.

Figure 1. Left: spherical probe with GEM-60 test bay and nozzle in the background. Right: External frame tetrahedral probe utilizing four matched condenser microphones. This probe is an inverted tetrahedron, where microphone 1 is beneath the horizontal plane containing microphones 2, 3, and 4.

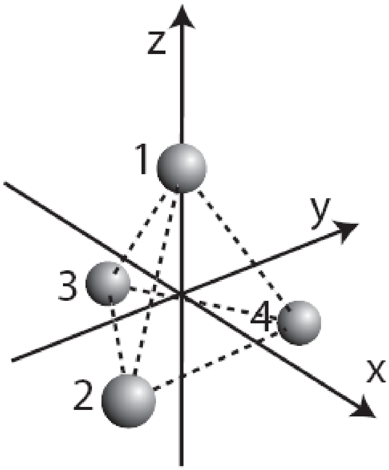

Figure 2. Tetrahedral probe geometry, where microphones 2 and 4 are parallel to the y axis.

III. Experiment Setups

The 16.2-m GEM-60 motor has a 1.52-m (60-in) diameter graphite epoxy case and burns a solid propellant cast at ATK. The nozzle exit diameter, *D*, is 1.22 m (48-in); microphone locations are subsequently scaled in terms of this diameter. Two of these motors are used as boosters on Delta IV Medium launch vehicles and each produces a vacuum thrust of 827 kN (186,000 lbs.). Acoustical measurements of GEM-60 motor firings were made on 24 June 2008 and 19 February 2009 at the ATK T-6 test facility near Promontory, Utah. During the 6-24-08 test, the nozzle was gimbaled ±5° in both the horizontal and vertical directions. For the 2-19-09 test, the nozzle was fixed. The significant-thrust portion of the motor burn lasts approximately 85 s and the total burn length is about 90 s.

The two types of energy-based probes shown in Fig. 1 were deployed in the field along with other microphones as shown in Fig. 3. Filled markers are used to show locations of sensors during the 6-24-08 test. Because prior measurements of spalling of the concrete pad had revealed a spread rate of the plume of approximately 16° and because of the ±5° nozzle gimbaling, the angle of the sensor array was set to 22° relative to the plume centerline. The sensor locations included an offset from the presumed edge of the plume of 8.5*D* for the external frame tetrahedral probes and other microphones present in the near-field and a 6*D* offset for the spherical probe in order to more fully test the probe limits. The other microphones located parallel to the 22° line included 3.18-mm and 6.35-mm pressure microphones as shown in Fig. 3.

For the 2-19-09 test, four NASA spherical probe prototypes were deployed along with three external frame tetrahedral probes and other microphones. In order to characterize low frequencies more fully, the microphone separation on the external frame probes was increased such that the diameter of the sphere circumscribing the microphones was 0.054 m (2.0 in). The measurement array was located along a 20° angle relative to the centerline with a 7.5*D* offset from the edge of the plume. Displayed in Fig. 4 are photographs from this test showing the terrain variation to the left of the firing pad, the test bay, and the array being set up. Note that because the frozen ground precluded leveling of the tripods, the sensors were adjusted on the tripods so that they were approximately level.

For both tests, time data were sychnronously recorded using a National Instruments-based data acquisition system displayed in Fig. 5. The system consisted of a NI-8353 server and a PXI chassis containing PXI-4462 cards. These 24-bit cards have a maximum sampling frequency of 204.8 kHz and variable analog input ranges up to a maximum of ±42 V. A large voltage input range is required because pressures in excess of 20 kPa may exceed 10 V for the traditional condenser microphones.

Displayed in Figs. 6 and 7 are photographs of the 2-19-09 GEM-60 motor firing. The first photograph, shot from inside the test bay, shows the motor test stand and the plume as it spreads from the nozzle. In Fig. 7, a long-range view of the motor being fired is shown. This corresponds to nearly the end of the test, where the visible burning plume length is not as large as it had been nearer to the beginning of the test and the cloud rising from the plume is a couple hundred meters high. Circled in the photograph is a cluster of rocks, which serves as a frame of reference near which the 50*D* microphone was located.

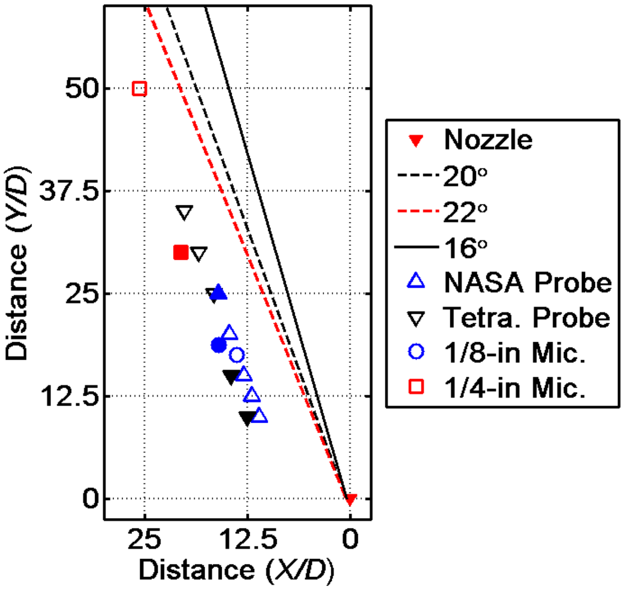

Figure 3. Near-field experiment setup for the 6-24-08 (filled markers) and 2-19-09 GEM-60 static firings at ATK. The 16° angle represents the nominal spread of the plume. The arrays were aligned along a 22° angle for the 6-24-08 test because of the nozzle gimbaling and along a 20° angle for the 2-19-09 test. The physical offsets from the angle lines drawn were 6 and 8.5*D* for the 6-24-08 test and 7.5*D* for the 2-19-09 test. Note that the positive x axis is to the right of the plume.

Figure 4. Photographs of near-field array during the 2-19-09 test setup. Top Left: View from near nozzle showing terrain variation. Top Right: View of the test bay shot from near the farthest external frame tetrahedral probe (35*D* downstream of the nozzle exit). Bottom: View of the test bay from just beyond the farthest near-field microphone (50*D* downstream of the nozzle exit). Cables from the array were run uphill to the rear of the test bay, where the recorder was located.

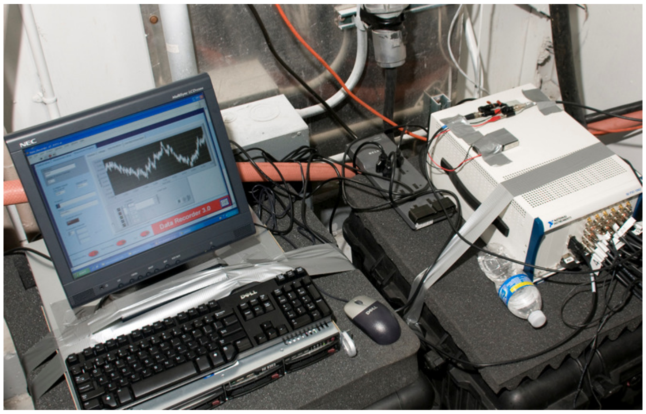

Figure 5. Recording system, consisting of a National Instruments 8353 server with monitor and peripherals and a PXI-1042 chassis. Time waveform data were recorded using PXI-4462 cards with a sampling rate of 204.8 kHz.

Figure 6. Photograph of the 2-19-09 GEM-60 static firing from inside the test bay.

Figure 7. Photograph near the end of the 2-19-09 static firing, where the length of the visible flame is considerably shorter than at the beginning of the test. Circled is a cluster of rocks that were approximately 55*D* downstream of the nozzle. The 50*D* microphone pictured at the bottom of Fig. 4 was near these rocks.

IV. Spectral, Waveform, and Statistical Results

Before describing intensity-based results, the relative rarity of near-field rocket noise data and the need to examine the performance of these probes suggests that an in-depth analysis of more traditional measures of acoustic levels and a comparison of the two motor firings is merited.

A. Overall Levels and Spectrogram for 6-24-08

First displayed in Fig. 8 is the OASPL at 15*D* downstream from the nozzle for the 6-24-08 test. Also displayed are the theoretical thrust profile (represented logarithmically in "decibels") and the nozzle gimbaling pattern. The overall level and the thrust profile track very well during the significant thrust portion of the motor firing. In addition, the fluctuations in level primarily track the horizontal movement of the nozzle, recognizing that a positive nozzle angle is to angle the flow field toward the measurement array. The vertical nozzle gimbaling also plays a role in the level fluctuation. Note that the fluctuations after 20 s are greater in level when the horizontal and vertical patterns are nearly in phase. Fig. 9 shows the spectrogram from the overall levels shown in Fig. 8. The fluctuations due to the nozzle movement and, to a lesser extent, the thrust profile, are apparent. Overall, however, the spectral shape remains consistent throughout the test.

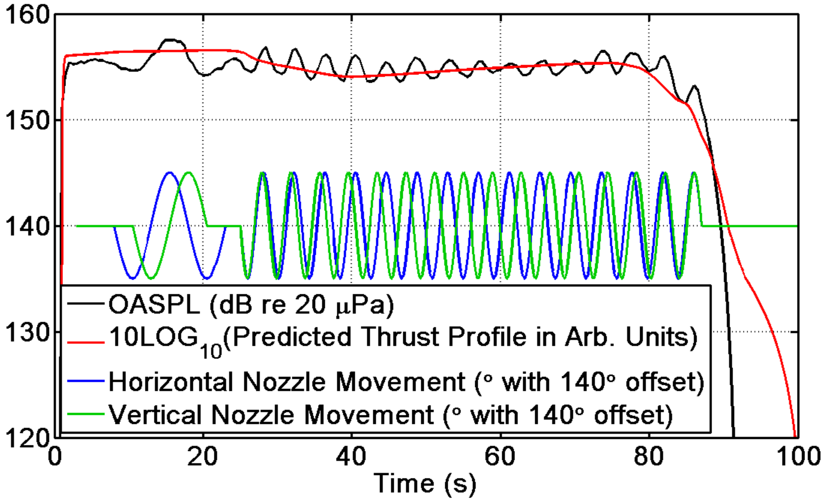

Figure 8. OASPL as a function of time 15*D* downstream along with an accompanying scaled figure of the logarithmic thrust profile of the motor. Also shown are the ±5° horizontal and vertical nozzle gimbaling schedules about 140° offset with a 3.5 s delay in time to account for the OASPL lag.

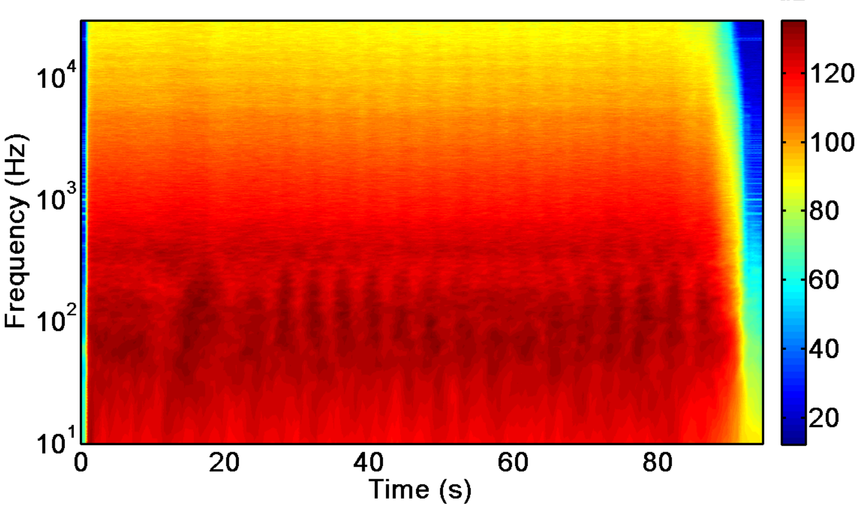

Figure 9. Spectrogram for the 6-24-08 test at one of the spherical NASA probe prototype microphones located 15*D* downstream of the nozzle exit.

B. Comparison of OASPL and Power Spectral Densities between Firings

As stated before, the primary difference between the 6-24-08 test and the 2-19-09 test was the fixed nozzle during the latter firing. Displayed in Fig. 10 are the overall levels during the two firings at microphones located 15*D* downstream from the nozzle exit. The curve for the earlier test is the same as shown in Fig. 8. Note that the microphone for the 2-19-09 test is approximately 1 m closer to the nozzle centerline than the 6-24-08 microphone. However, given the source length and the offset from the plume, this is not thought to create a significant difference in level. Again, the variation in level throughout the test tracks very well with the logarithmic thrust profile shown previously in Fig. 8. This result helps establish the consistency between the two tests.

Not every aspect of the measurements was the same, however. A very significant difference between the two firings was the ambient temperature (differing by about 20° C) and the ground effect. Although the temperature effect is not likely to make a large difference in the near field due to the high temperatures encountered at the microphones (>50° C), the change in ambient temperature could result in differing refractive effects as the sound speed varies in the surrounding medium. The change in the local terrain, however, is a different story. Significant snowfall (~0.5 m deep on the hillside) prior to the 2-19-09 test resulted in much softer ground impedance than the rock-like terrain encountered in the 6-24-08 test. This, in turn, resulted in interference nulls that occurred at lower frequencies for microphones located at similar points in the field. This phenomenon is shown in Figs. 11 and 12 for microphones located 15*D* and 25*D* downstream from the nozzle. At 15*D*, the interference null has shifted from about 250 Hz to 100 Hz, effectively removing the spectral peak from the power spectral density. At 25*D* (see Fig. 11), the interference nulls for both tests occur at higher frequencies because of the smaller difference between the direct and the ground reflected paths; however, the lower frequency null due to the snow-covered terrain in the 2-19-09 data is readily apparent.

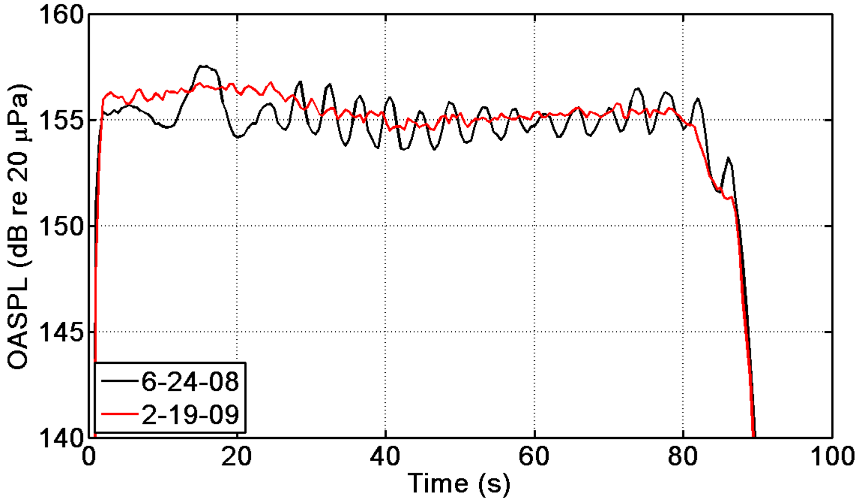

Figure 10. Comparison of OASPL as a function of time for the two firings 15*D* downstream.

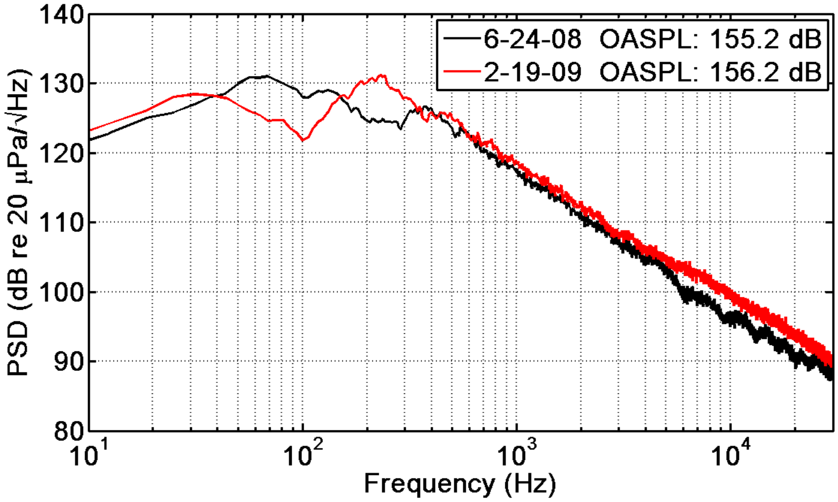

Figure 11. Comparison of power spectral densities measured 15*D* downstream for the two tests.

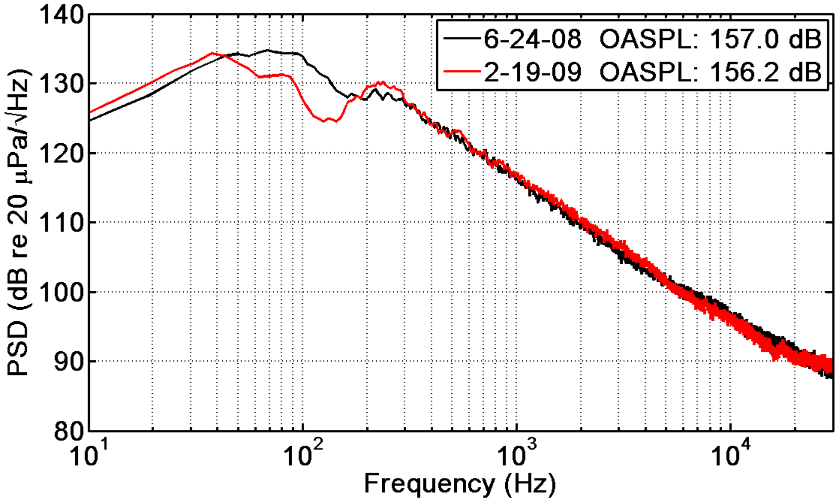

Figure 12. Comparison of power spectral densities measured 25*D* downstream for the two tests.

C. Near-field Spectral Results as a Function of Distance

The OASPL from the near-field array for the 2-19-09 test is displayed in Fig. 13. Note that, extrapolating the trend from 10*D* to the nozzle exit plane, a 3-dB drop in overall source level occurs over a distance of nearly 40*D*, or approximately 50 m. This represents a very large source region. Because the overall level does not reveal the frequency dependence of level with distance downstream, the PSD from each of the locations displayed in Fig. 13 is plotted in Fig. 14. The significant ground interference null is readily apparent in the measurements, but below and above this region, some trends may be noted. Low frequency levels grow with distance downstream, whereas the high frequency levels decay with distance. This is not unexpected, since higher frequencies are generated closer to the nozzle than lower frequencies. Although very informative in their own right, scalar-based plots like Figs. 13 and 14 cannot address the directionality of the sound radiation of the source as it passes through the near-field array. Vector acoustic intensity can be used to investigate this question and is the subject of the remaining analysis in this paper.

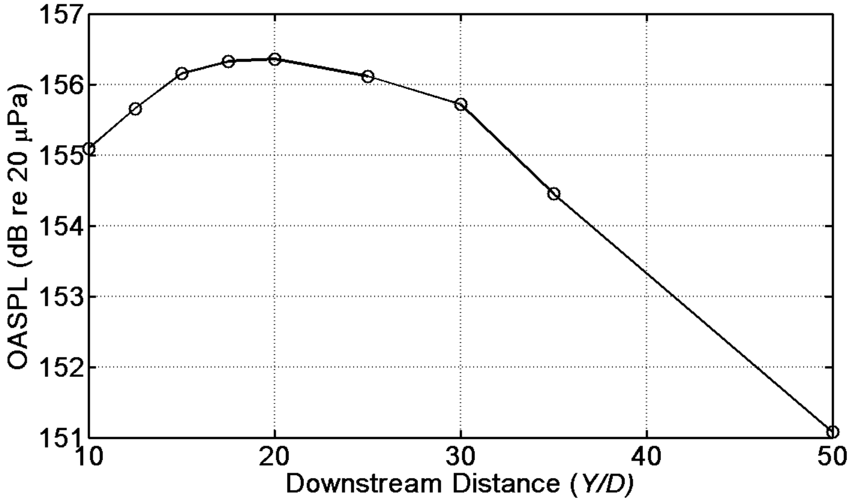

Figure 13. Near-field overall sound pressure level as a function of distance downstream during the 2-19-09 GEM-60 firing at ATK.

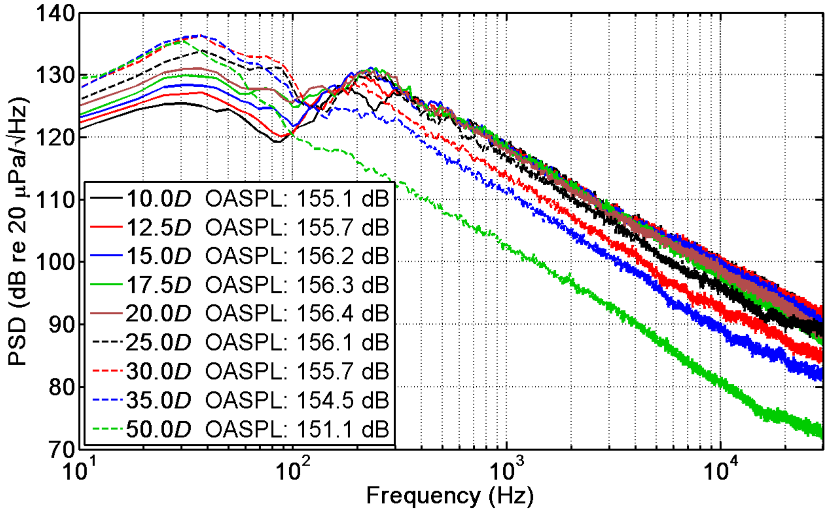

Figure 14. Power spectral densities in the near-field during the 2-19-09 GEM-60 firing.

V. Vector Probe Analyses

In this section, data collected with both types of vector probes are examined using spectral, statistical, and time waveform analyses. The purpose of this examination is to study the general quality of the acoustic data acquired by the multi-microphone sensors.

A. NASA Spherical Probe Performance Analysis

The spherical probe prototype shown in Fig. 1 recorded data during the the 6-24-08 GEM-60 firing. Power spectral density results from the first 10 s of the motor burn are displayed in Fig. 15. Microphones 2 and 4 (channels 9 and 11 in Fig. 15) were oriented along the y-axis, meaning that microphone 2 (channel 9) essentially faces the plume. Microphone 3 (channel 10 in Fig. 15), on the other hand, is at the rear of the sphere, toward the negative x axis. Microphone 1 and possibly microphone 4 (channels 8 and 11) are essentially at grazing incidence to the propagating sound field. The relative locations of the microphones can largely explain the diverging spectral trends in Fig. 15 above 1 kHz. Microphone 2 (channel 9) faces the sound field, which is a nonideal orientation for a pressure microphone (as is the GRAS 40BH). Coupled with the effects of scattering off and around the sphere, this results in excess high-frequency levels. Microphone 3 (channel 10) is located behind the sphere. Appreciable shielding effects of the sphere above 5 kHz, where the 2.54 cm diameter sphere becomes a significant fraction of a wavelength, causes the high frequency levels to be reduced. On the other hand, microphones 1 and 4 have the "cleanest" and nearly identical spectral roll-offs, which are similar to the familiar f^{-2} slope expected at high frequencies for supersonic jet and rocket noise. It is supposed that this is because the microphones are nearly ideally oriented relative to the sound field propagation direction.

A time domain analysis of the data is also revealing. Examination of short sections of the time waveforms recorded by the four microphones in Fig. 16 and a further zoomed-in portion in Fig. 17 shows, first, the similarity of the data on a broad scale, and second, small differences that reveal themselves in Fig. 17. Recalling that the data are simultaneously sampled, the same shock incident on the probe arrives at the individual microphones at slightly different times. This gives rise to the ability to determine propagation direction. In addition, note the similarities of the responses of microphones 1 and 4 (channels 8 and 11) and the differences of microphones 2 and 3 (channels 9 and 10, respectively). Shocks incident on microphone 2 have much larger positive values. This is primarily due to diffraction effects and the pressure microphone at normal incidence to the field. Similar results were reported by Gabrielson *et al.*[10] in their study of weak-shock measurements. The shock that arrives at microphone 3, on the other hand, has a different shape than the other microphones with a greater rise time; this is certainly caused by the shielding, low-pass filter effects of the sphere.

Displayed in Figs. 18 and 19 are the results of statistical analyses of the time waveforms. The probability density functions of the time pressure reveal the average differences between the sound arriving at the four microphones (Fig. 18), whereas the probability density functions of the first-order time derivative of the pressure (Fig. 19) reveal the differences between changes in pressure. Estimation of the probability density functions permits the average impact of the sphere on shock rise times to be seen. Displayed in the legend of each figure is the skewness (a measure of asymmetry) of the distribution for each microphone. For the distribution of the pressure in Fig. 18, microphones 1 and 3 and 4 behave similarly, whereas the distribution for microphone 2 is more positively skewed (as was evident in the time domain results in Fig. 16 and 17). The result for microphone 3 suggests that the sphere does not significantly impact the distribution of pressures measured. On the other hand, Fig. 19 shows that the sphere does impact the rise time of the shocks, which are represented in the positive tail of the distribution and the skewness calculation. To summarize the results in this section, it appears that the probe microphones may be used as quality transducers for other purposes than energy-based measurements. Although the presence of the sphere and the possibility of nonideal orientation of one or more microphones impact high-frequency measurements, the "average" data appear fairly clean.

This analysis of probe performance does not include investigations of the amplitude and phase matching of the microphones, which is important to the estimation of particle velocity. Testing of the probes in a plane-wave tube showed linearity of the phase relationship above approximately 100 Hz. Below 100 Hz, amplitude and, more importantly, phase mismatch between the channels began to play a role. The plane-wave tube technique was utilized to develop calibration curves for the probes at low frequencies that are applied in the post-processing to improve the matching between channels. This calibration approach causes the probes' effective range for energy-based calculations to be valid down to approximately 50 Hz.

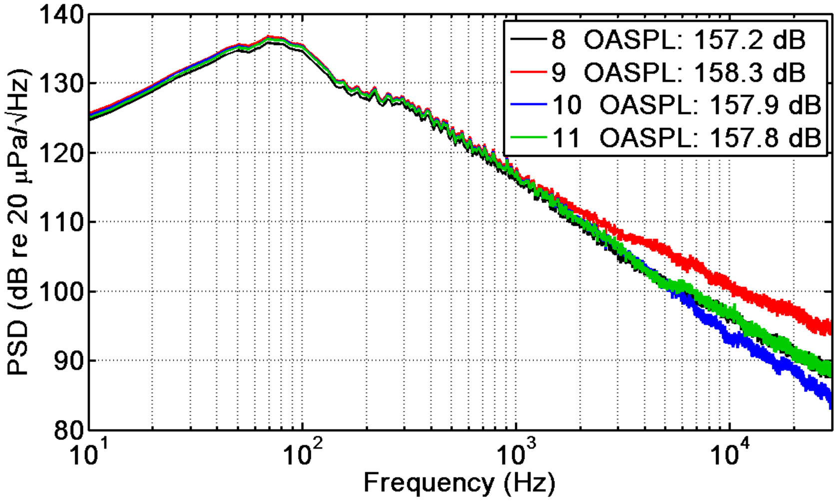

Figure 15. Power spectral densities for the four spherical probe microphones during the 6-24-08 test 25*D* downstream of the nozzle. Channels 8-11 correspond to microphones 1-4 in Fig. 1, respectively.

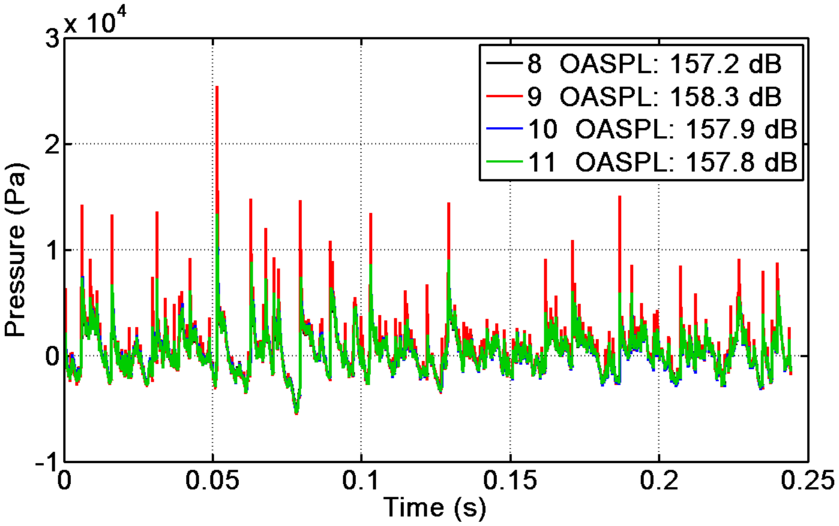

Figure 16. **Segments of the waveforms measured at the four microphones on the spherical probe. From this broad look, the waveforms are very similar and suffer only from some amplitude differences at the shocks. The OASPL values here refer to the 10-s portion of the waveform used to calculate the PSD in Fig. 15, not this small segment.**

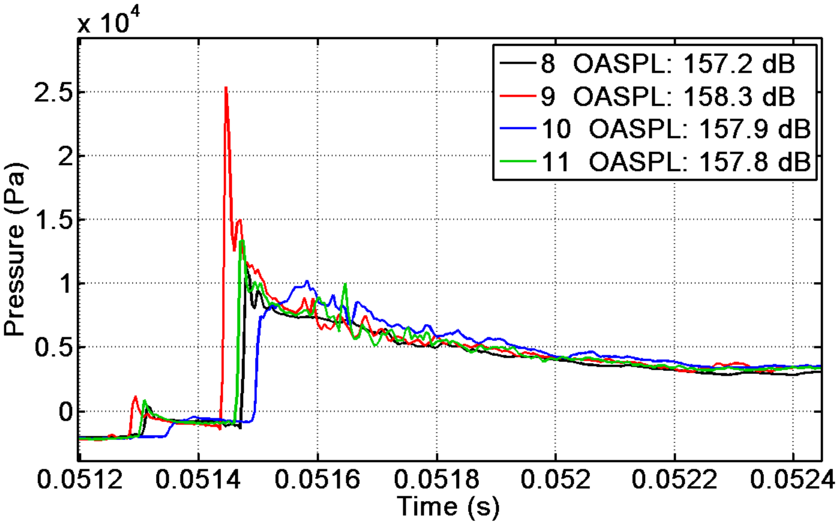

Figure 17. A smaller portion of the waveforms in Fig. 16, revealing the slight timing difference between the microphones (due to the propagation delay) and the microphones' different responses to a high-amplitude shock.

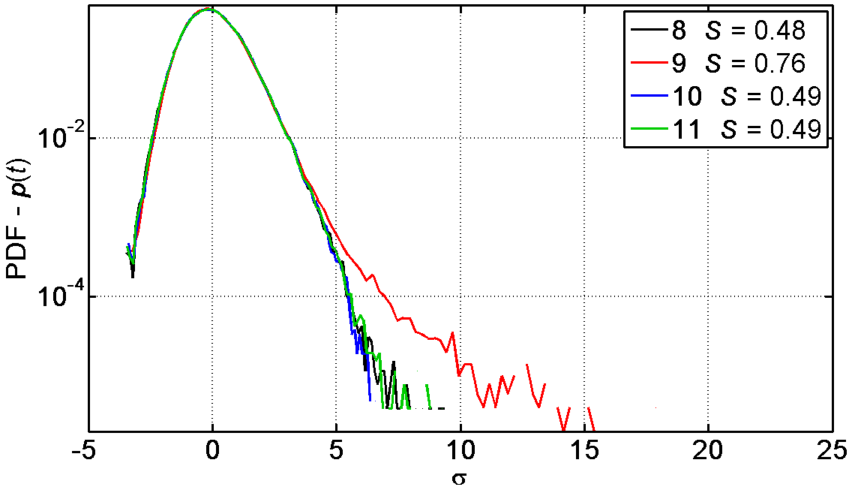

Figure 18. Probability density functions, represented on a log scale and normalized in terms of number of standard deviations, *σ*, and calculated using 10 s of waveform data at the spherical probe microphones. Microphone 2 (channel 9) yields a greater positive tail and greater skewness, *S*, which are caused by the shock amplitudes being overestimated.

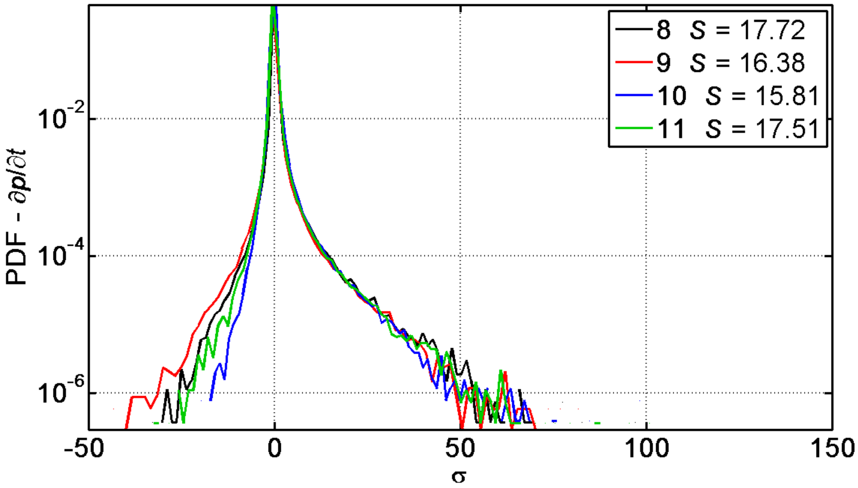

Figure 19. Probability density function of the first-order time difference of the waveform data, normalized in terms of the number of standard deviations, *σ*. The greatest difference between the microphones occurs at the tails, where the positive tail represents the large values represent the rapid pressure changes encountered at a shock.

B. External Frame Tetrahedral Probe Performance Analysis

An analysis similar to the preceding section can be performed on the external frame tetrahedral probe. This probe is fundamentally different than the spherical probe in that the propagating wavefronts can pass directly through the center of the probe. Consequently, one would expect the scattering off this probe to be quite different than that off the spherical probe. The PSDs in Fig. 20 confirm this in that there is slight ringing and there are only minor differences between the spectral responses up to nearly 10 kHz, at which point microphone 3 (channel 6) diverges upward and microphone 2 (channel 5) diverges downward. This is exactly the opposite situation as with the spherical probe, because these microphones point inward toward the origin of the probe, whereas the microphones on the spherical probe point outward from the origin. Microphone 3 is nearly facing the propagating sound field and the wavefronts incident on microphone 2 are subject to appreciable diffraction around the preamplifier housing before reaching the microphone diaphragm.

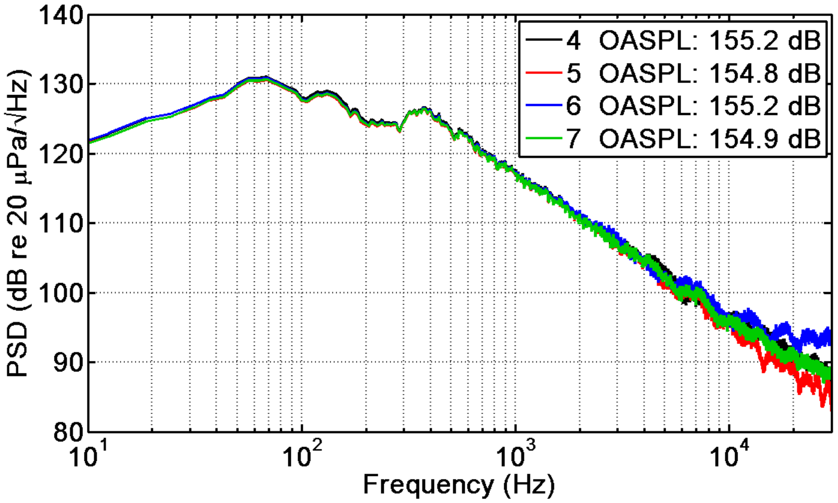

Figure 20. Power spectral densities measured at an external frame tetrahedral probe. Channels 4-7 represent microphones 1-4 in Fig. 1, respectively.

Examination of time waveform segments recorded by the external frame probe in Figs. 21 and 22 reinforce the concept that, like the spherical probe, the microphone pointing towards the sound field appears to overestimate the shock amplitude. However, the microphone pointing away from the sound field (channel 5) is not as significantly impacted as with the spherical probe. This is presumably because the 6.35-mm diameter microphone preamplifier housing does not present as large an obstruction to the sound field as a 2.54-cm diameter sphere. The statistical results in Figs. 23 and 24 confirm that microphones 1, 2, and 4 (channels 4, 5, and 7) give nearly identical results in terms of the distribution of pressure values and the change in pressure with respect to time. Microphone 3, on the other hand differs significantly from the other microphones for both the pressure and its time derivative estimate. This difference is more extreme than for the spherical probe. In particular, the skewness of the time derivative estimate is greatly reduced because of a large number of negative values. These values stem directly from the fact that a shock is followed immediately by a steep negative value, which greatly reduces the overall skewness of the distribution. The likely cause of this is the nonideal orientation of this microphone in the sound field, since pressure microphones are intended to be set at grazing incidence to the propagating sound field.

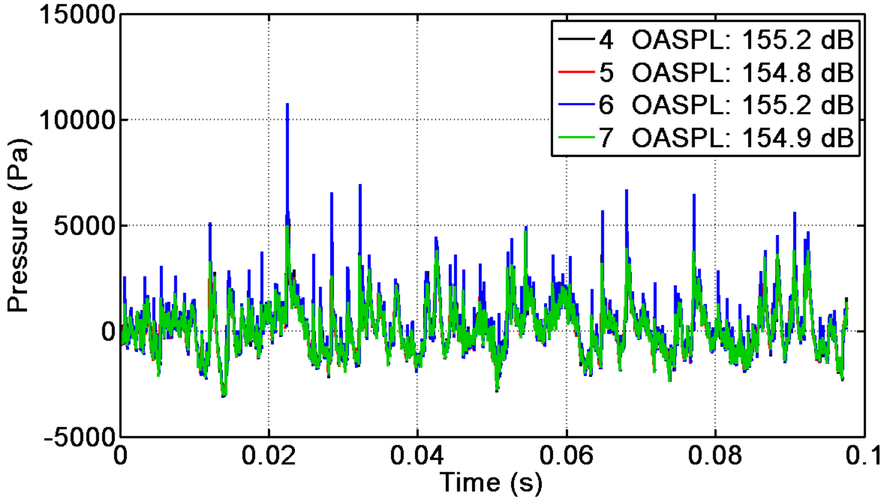

Figure 21. Time waveform segments measured by microphones mounted on the external frame tetrahedral probe. The OASPL refers to the entire 10-s waveform used in the spectral analysis.

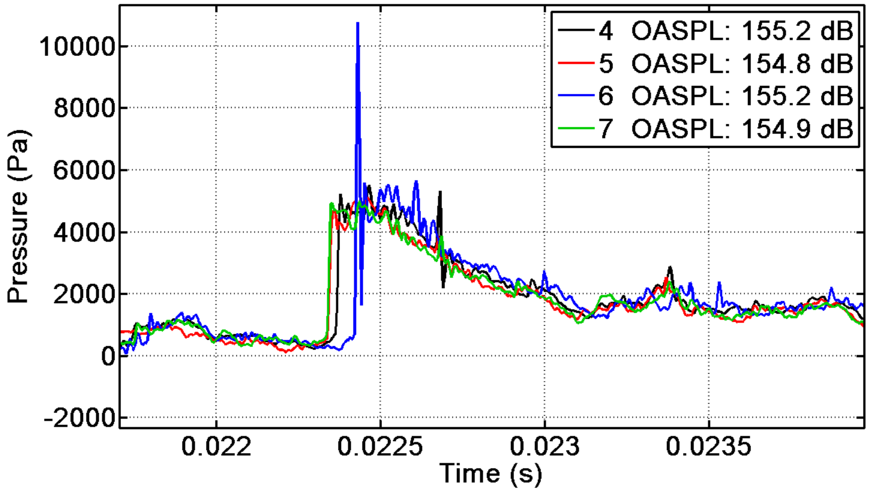

Figure 22. Zoomed-in portion of the waveform segment in Fig. 21. The overestimation of the shock amplitude at microphone 3 (channel 6) is because of the pressure microphone being at near normal-incidence to the sound field.

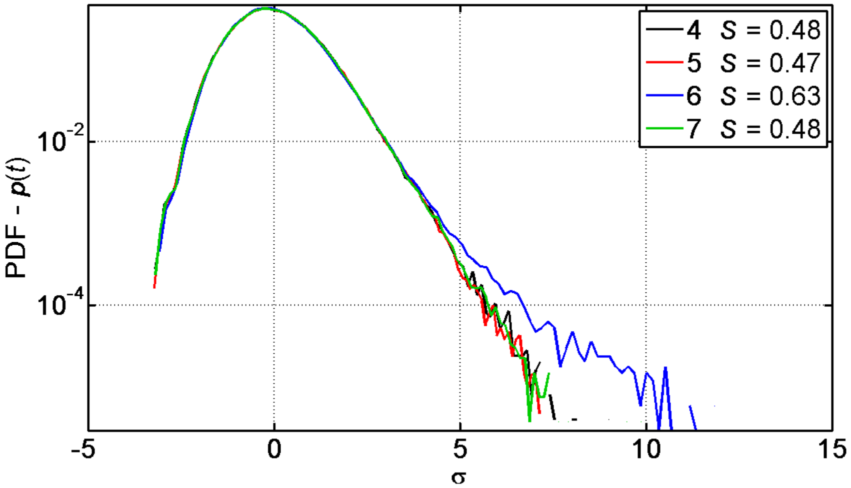

Figure 23. Probability density functions of the pressure waveforms for all four external frame tetrahedron microphones. As with the spherical probe, the microphone at normal incidence (microphone 3/channel 6) has the large positive tail, which is caused by overestimation of the acoustic shock amplitudes.

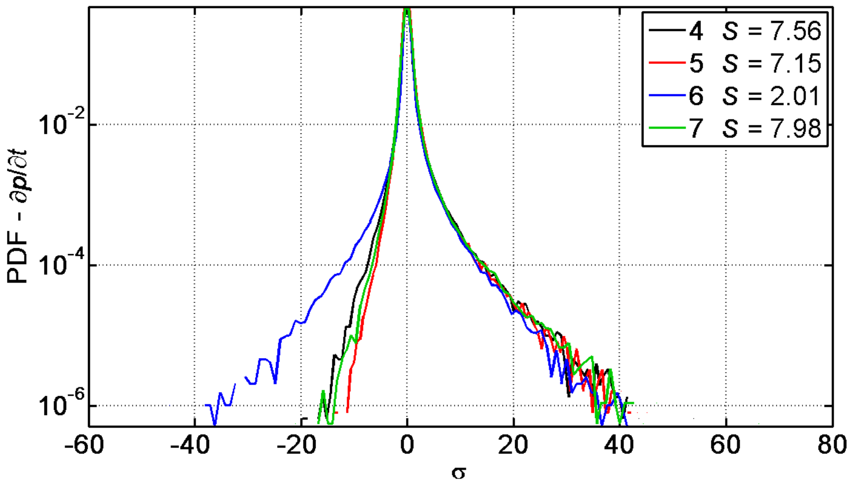

Figure 24. Probability density functions of the first-order time difference of the four external frame tetrahedron microphones. The large negative tail for microphone 3 (channel 6) results in a substantially different skewness than for the other four microphones. This tail is caused by the dips that immediately follows shocks (see Fig. 22) and is due to microphone diffraction around the pressure microphone diaphragm for nonideal incidence.

In order to use the tetrahedral probes as vector probes at low frequencies, amplitude and phase calibrations were carried out using a GRAS 51AB intensity calibrator. A simpler approach was available than the plane-wave tube technique implemented for the spherical probe because the microphones can be easily removed from the tetrahedral frame. The intensity calibrator presents the same acoustic field to both microphones, allowing the phase and amplitude mismatch between channels to be determined and corrected in post-processing. This calibration was carried out to as low as 40 Hz for all three tetrahedral probes but was found to only be needed in the 40BH-based tetrahedral probe. The prepolarized microphones were sufficiently matched to yield their direct use for the sensor separation distances employed down to below 50 Hz.

VI. Vector Intensity Measurement Results

A. Spatial Vector Intensity

As described in Fig. 3, the two types of energy-based probes were deployed for the 6-24-08 and the 2-19-09 GEM-60 firings. Three probes (one spherical probe and two prepolarized external frame tetrahedral probes) were placed during the 6-24-08 firing and seven probes (four spherical probes and three external frame tetrahedrons) were used for the 2-19-09 firing. The intent was to position probes for the 2-19-09 test near where they had been located for the 6-24-08 firing to determine consistency of results.

Displayed in Fig. 25 are X-Y intensity vectors for a number of different frequencies as viewed from above the plume. The nozzle and presumed plume edge are shown in the figures for reference. Amplitudes of the vectors are scaled relative to each other for each frequency, not on an absolute scale over all frequencies. The amplitude of each vector in a given plot is scaled according to the square root of the intensity magnitude at that frequency. At 50 Hz, it is apparent that this low frequency is generated relatively far downstream. The intensity vectors also reveal the directionality of the sound radiation at that frequency. The probe located 20*D* downstream has a vector, which points towards, rather than away from, the source. A check of this probe reveals that it has the largest phase corrections required of any of the probes at low frequencies. In other words, this result is very likely caused by residual phase mismatch between microphone channels on that probe due to imprecise phase corrections applied in post-processing. Between 50 and 150 Hz, the results are not shown because they fall within the frequency region where the ground interference null for the 2-19-09 test was most significant. Between 150 and 300 Hz, the region of dominant acoustic intensity moves upstream while maintaining a similar directionality of the radiation. The results from 500 Hz to 3000 Hz are extremely similar, suggesting that the aeroacoustic source mechanism is similar for these frequencies; i.e., they radiate with similar directional characteristics and from similar locations.

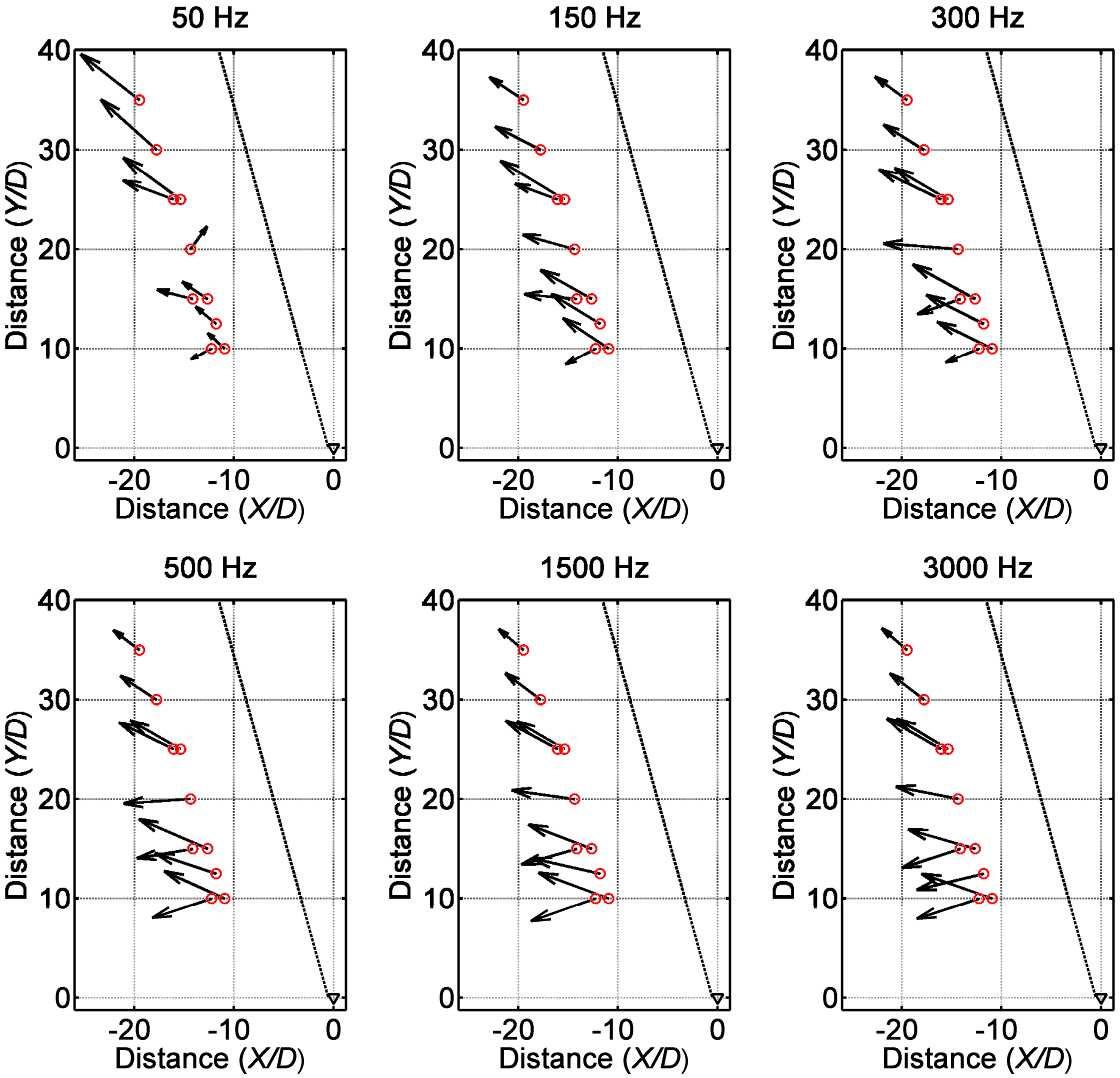

Figure 25. 10-s average of X-Y intensity after motor ignition. The nozzle is located at the origin and the line represents the estimated edge of the plume.

What has not been discussed is the rapid change in direction associated with the probe locations upstream of 20*D*. With the 7.5*D* offset, where the data were taken on 2-19-09, the noise appears to essentially be radiating away from and downstream at most probe locations and frequencies. At the probe locations with the 8.5*D* offset from the plume (from the 6-24-08 test), the noise largely appears to radiate away from and upstream of the nozzle. Although some uncertainty in probe positioning and alignment in the field is probable, the 30° or so difference between the direction of propagation at 7.5*D* and 8.5*D* being solely due to probe orientation errors is very unlikely. What, then, are other possible causes of these results? First, there is the possibility that these results are wholly physical, and these results represent the refraction due to an extreme temperature gradient over a short distance. (The radiated temperatures themselves are sufficiently extreme to partially melt cables and scorch duct tape close to the nozzle.) Second, the temperature gradient may have differed substantially between the June and February tests resulting in near-field propagation differences near the plume. Third, there is the possibility that terrain-related effects resulted in these differences. These microphones were located on a hill of moderate slope. The microphones during the 2-19-09 test would have been located more on the side of the hill than on the top, which was the case during the 6-24-08 test. Also, as noted before the ground impedance on the hill where these tripods were placed would have varied substantially during the two tests. The heating of the ground, a contributor to the temperature gradient, would also have been different. It is also a possibility that the large pillars to the front of the test bay could have presented themselves as significant reflectors, which would impact microphones closer to the plume. Although the cause cannot be conclusively determined, it is, however, noted that the intensity angle for the probe 12.5*D* downstream is observed to vary significantly as a function of frequency and time, but essentially between the angles given at 10 and 15*D*. Consequently, it appears that these results are primarily caused by differences in near-field propagation close to the nozzle between the two tests and/or rapidly changing directions of propagation as a function of space.

As shown previously, the thrust of the motor varied as a function of time. It is reasonable to expect the source region to contract or move upstream during periods of lesser thrust. Displayed in Fig. 26 are horizontal intensity vectors, similar to Fig. 25, but during a period beginning 50 s after motor ignition. It is clear that some of the conclusions discussed previously are the same. In particular, note that the dominant intensity vector locations move upstream as a function of frequency, but that the results above 500 Hz are very similar. In comparing Figs. 25 and 26, however, it is clear that the angle of propagation, relative to the x-axis, has generally lessened. This means that the source region has moved somewhat upstream and/or the directionality of the radiation has changed. Also note that when comparing high-frequency results (e.g., 3000 Hz), the source region appears to have contracted in length 50 s into the test because the vectors at 25, 30, and 35*D* are shorter in length relative to those at the beginning of the motor burn. Finally, it is worth comparing the angular variation of the vector for the probe located 20*D* downstream of the nozzle. In Fig. 25, this vector shows sound nearly propagating along the negative x axis from 500 Hz and above. As frequency increases, the angle lessens, suggesting that the dominant noise source is now upstream of the source. In Fig. 26, the angle also lessens slightly, but now points in a direction for all three frequencies suggesting that the dominant source is upstream of that location.

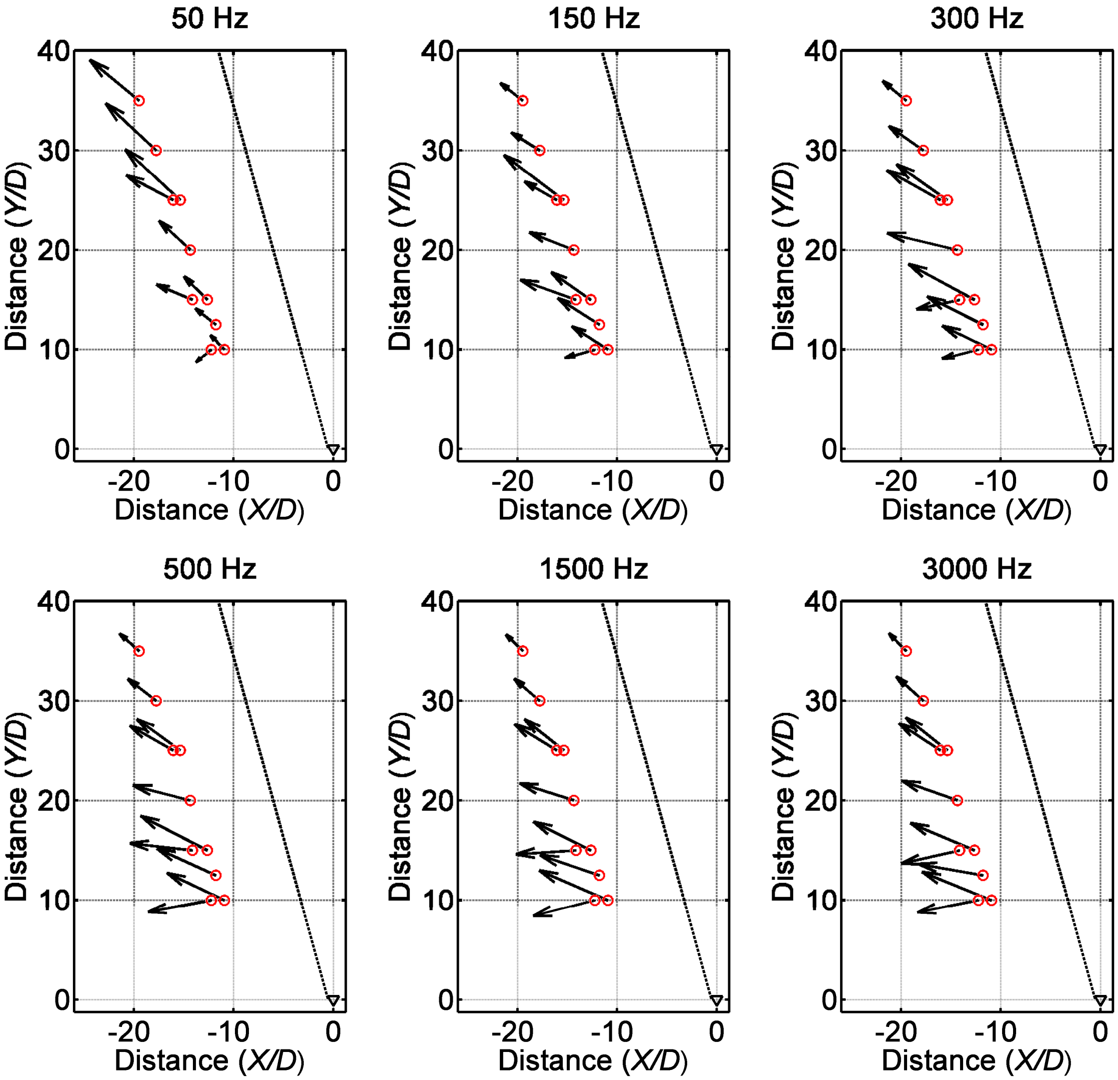

Figure 26. 10-s average of X-Y vector intensity beginning 50 s after motor ignition.

B. Frequency-Averaged Intensity Angles as a Function of Time

Figures 25 and 26 showed variation in direction of propagation and source characteristics as a function of time. This concept is pursued further by comparing the frequency-averaged (50 Hz – 6 kHz) intensity angles as a function of time throughout the test using the 25*D* probes. These are calculated using 1 s blocks of data and stepping forward in 0.25 s increments. The results of these calculations are displayed in Fig. 27, which shows that the angular variation tracks the variation in thrust for both motor firings. In addition, the correlation between intensity angle and nozzle angular movement is clear, including the fact that the maximum short term variation in intensity angle for the 6-24-08 test appears to be on the order of 10°. The fact that there is an average 8° or so difference between the two probe results is evident in Figs. 25 and 26. It is not known if this average difference is caused by slight variations in source characteristics or errors in probe positioning and alignment. In any case, however, the results from the two different firings track very well, including the continual decrease in angle as the thrust gradually lessens at the end of the test. This again suggests a contraction of the aeroacoustic source region toward the nozzle.

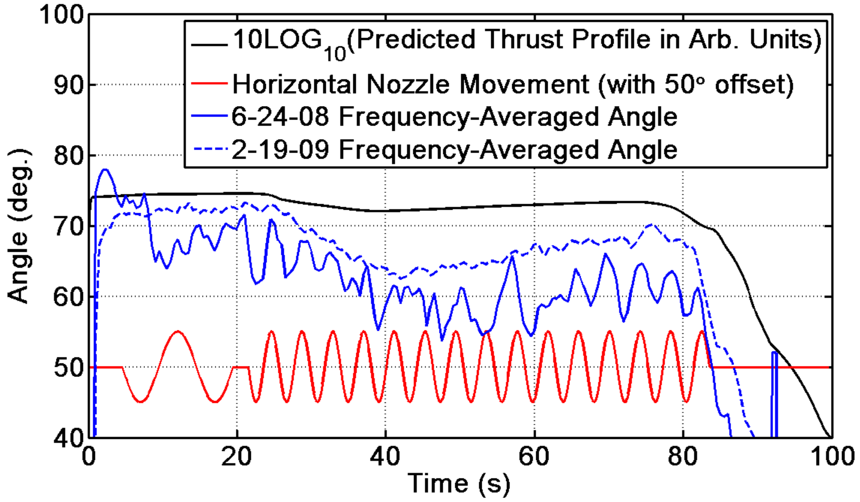

Figure 27. Frequency-averaged intensity angle (measured relative to the plume centerline) as a function of time during the firings 25*D* downstream of the nozzle. Shown also are the logarithmic motor thrust profile and the horizontal nozzle movement during the 6-24-08 test.

VII. Conclusion

This paper describes the successful application of vector intensity analysis to the measurement of rocket noise sources. Although there is much more to explore in terms of applications and meaning, an energy-based measurement approach can reveal more information about source characteristics than can traditional pressure measurements. For example, intensity vectors could be used to explore near-field refraction caused by temperature gradients as the sound energy travels from the source to the far-field. Further measurements to be made with the spherical probes include tests of the RS-68B engine, which, because it is not a solid-fueled motor, will not have as great of temperatures and will permit measurements to be made closer to the source and more in the acoustic near-field. Along with additional measurements, future work includes further development of hardware particularly optimized for lower frequencies but capable of broadband measurements. In addition, there is additional work to be carried out in the development of energy-based processing algorithms suitable for broadband propagating fields. Finally, vector-intensity-based source localization and characterization algorithms are being developed.

Acknowledgments

This research was carried out in conjunction with an STTR with STI Technologies funded by NASA Stennis Space Center. The authors also express their deep gratitude to Mr. Roy Norris of ATK Test Services for his assistance with and facilitation of the measurements. Finally, the authors acknowledge members of the BYU Acoustics Research Group for their help in setting up the field measurements and to Daniel Manwill for fabrication of the external frame tetrahedral probe holders.

References

[1]Fahy, F. J., *Sound Intensity*, 2nd ed., E&FN Spon, London, 1995.

[2]Jaeger, S. M. and Allen, C. S., “Two-Dimensional Sound Intensity Analysis of Jet Noise,” AIAA paper 93-4342, October, 1993.

[3]Ventakesh, S. R., Poak, D. R., and Narayanan, S.,“Beamforming Algorithm for Distributed Source Localization and its Application to Jet Noise,” *AIAA Journal*, Vol. 41, No. 7, 2003, pp. 1238-1246.

[4]Yu, C., Zhou, Z., Zhuang, M., “An Acoustic Intensity-Based Method for Reconstruction of Radiated Fields,” *Journal of the Acoustical Society of America*, Vol. 123, No. 4, 2008, pp. 1892-1901.

[5]Yu, C., Zhou, Z., Zhuang, M., “An Acoustic Intensity-Based Inverse Method for Sound Propagations in Uniform Flows, AIAA paper AIAA-2007-3563, May 2007.

[6]Cazzolato, B. S., and Ghan. J., “Frequency Domain Expressions for the Estimation of Time-Averaged Acoustic Energy Density,” *Journal of the Acoustical Society of America*, Vol. 116, No. 6, 2003, 3750-3756.

[7]G. Rassmussen, “Measurement of Vector Fields,” in *Proceedings of the 2nd International Congress on Acoustic Intensity*, 1985, pp. 53-58.

[8]Santos, I. M. C., Rodrigues, C. C., and Bento Coelho, J. L., “Measuring the Three-Dimensional Acoustic Intensity Vector with a Four-Microphone Probe,” in *Proceedings of Inter-Noise 89*, 1989, pp. 965-968.

[9]Thomas D. C., “Theory and Estimation of Acoustic Intensity and Energy Density,” M.S. Thesis, Department of Physics and Astronomy, Brigham Young University, Provo, UT, 2008.

[10]Gabrielson, T. B., Marston, T. M., and Atchley, A. A., “Nonlinear Propagation Modeling: Guidelines for Supporting Measurements,” *Proceedings of Noise-Con 2005*, 2005, paper nc05_193.